HAKIV: A MODULAR MPC-BASED AOCS FOR VLEO

B. Jäger*, F. G. Aloisio†
* Technische Universität Berlin, Chair of Space Technology, Marchstraße 12–14, 10587 Berlin, Germany
† EnduroSat GmbH, AOCS Department, Cuvrystraße 51-52, 10997 Berlin, Germany

Abstract

Very Low Earth Orbit (VLEO, below 450 km) offers substantial payload benefits for Earth observation and communications but imposes markedly higher demands on the attitude and orbit control system: atmospheric drag orders of magnitude larger than in conventional LEO, strong solar-activity-driven density variation, and physically coupled attitude and orbit dynamics through the shared aerodynamic environment. HAKIV develops a modular, software-defined, MPC-based AOCS spanning the 6U CubeSat to 100 kg SmallSat class to address this coupling.

This paper characterizes the VLEO disturbance environment across three satellite classes and the 200-450 km altitude band, and derives disturbance rejection requirements without presupposing specific hardware. Peak torque and thrust, disturbance bandwidth, reaction wheel momentum accumulation, and orbit determination bounded correction cadence are quantified as functions of altitude, satellite class, and solar activity. Torque bandwidth switches between magnetic and aerodynamic dominance at an altitude that itself shifts with solar activity. Orbit correction cadence is bounded not by actuator capability but by orbit determination precision.

A scale-invariant aerodynamic stiffness ratio Λ compares the aerodynamic lever arm disturbance across platform sizes, complementing a purely geometric radius of gyration normalization and identifying where aerodynamic torque dominates the characteristic inertial-orbital torque scale.

These results consolidate into four requirements: peak actuator authority, attitude control bandwidth, reaction wheel desaturation time, and orbit correction cadence with impulse capacity. The paper stops short of an uncertainty quantification of the disturbance environment and of actuator sizing/selection, both left as next steps toward a modular, holistic VLEO AOCS for small satellites.

Keywords

VLEO; AOCS; Disturbance Environment Modeling; Attitude-Orbit Coupling; MPC; Small Satellites

NOMENCLATURE

Formula symbols

bw_{95}	95%-cumulative-power bandwidth	Hz
δ_{OD}	orbit-determination precision	m
Δv_{ctrl}	required Δv per cycle at T_{ctrl}	m/s
H_{sat}	reaction wheel momentum capacity	Nms
I_{max}	max. moment of inertia	kg m^2
L, $\tilde{L}$	CoP-CoM lever arm, dimensionless	m, -
Λ	aerodynamic stiffness ratio	-
n	orbital mean motion	rad/s
τ_{peak}, F_{peak}	peak disturbance torque & thrust	Nm, N
q	dynamic pressure	Pa
τ_{aero}	aerodynamic disturbance torque	Nm
τ_{total}	vector-sum disturbance torque	Nm
T_{ctrl}, f_{ctrl}	min. ctrl. interval, max. ctrl. freq.	s, Hz
T_{sat}, f_{desat}	max. sat. interval, min. desat. freq.	s, Hz

Abbreviations

AOCS	Attitude and Orbit Control System
CoM	Center of Mass
CoP	Center of Pressure
F10.7	10.7 cm solar radio flux index (sfu)
HAKIV	Holistic AOCS for SmallSats in VLEO
MPC	Model Predictive Control
PSD	Power Spectral Density
SRP	Solar Radiation Pressure
VLEO	Very Low Earth Orbit

1. INTRODUCTION

1.1. The Pull Toward VLEO

Very Low Earth Orbit (VLEO, below 450 km) offers significant advantages for Earth observation (EO)

CC BY 4.0

doi: 10.25967/680492

and satellite communications (COMS). Lower altitude improves optical resolution, increases the received power of active sensors such as radar and lidar, and reduces communication path loss and latency [1]. VLEO also benefits from natural debris mitigation through atmospheric drag, a lower radiation environment that supports commercial-of-the-shelf (COTS) components, and higher launch capacity to lower altitudes. In addition, the residual atmosphere enables aerodynamic attitude and orbit control and may eventually serve as a propellant source for atmosphere-breathing propulsion [1, 2].
The feasibility of sustained VLEO operation was demonstrated by European Space Agency's (ESA) GOCE mission, which operated for more than four years at around 255 km and down to 229 km using continuous autonomous drag compensation [3]. With current VLEO activities increasingly centered on replenishable constellations, the focus is shifting from highly optimized individual spacecraft toward scalable, series-producible platforms.

1.2. The Catch: Payload Advantage, but Bus Difficulty

The payload benefits of VLEO come at the expense of a significantly more demanding spacecraft bus. At 200–400 km, atmospheric drag is orders of magnitude higher than in conventional LEO and must be continuously compensated despite strong density variations driven by solar and geomagnetic activity [4]. Aerodynamic disturbance torques can be orders of magnitudes larger, while faster ground tracks, sparse ground-station contacts, and tighter position-knowledge requirements further increase the demands on the Atitude & Orbit Control System (AOCS) [5]. The atmosphere nevertheless provides opportunities through active aerodynamic control and drag-assisted end-of-life disposal.
Today, VLEO AOCS are typically individually engineered for each spacecraft and orbit, an approach that does not scale economically or in development time to series-produced constellations. HAKIV therefore targets a scalable, software-defined AOCS that transfers VLEO-specific control capabilities into a reusable product across spacecraft classes and missions.

2. THE HAKIV PROJECT

2.1. Goal, Partners, and Development

HAKIV (Holistic AOCS for SmallSats in VLEO) develops a modular, scalable, and software-defined AOCS for spacecraft from the 6U CubeSat class to 100 kg. Funded by the German Space Agency at DLR and coordinated by EnduroSat, the project involves TU Berlin as research partner and e:fs TechHub as a subcontractor for predictive control technology. The funded work targets a laboratory demonstrator progressing from technology readiness level (TRL) 3 to TRL 5, with scalability, VLEO/LEO suitability, series production, European technological sovereignty, and EO and COMS applications as key constraints.

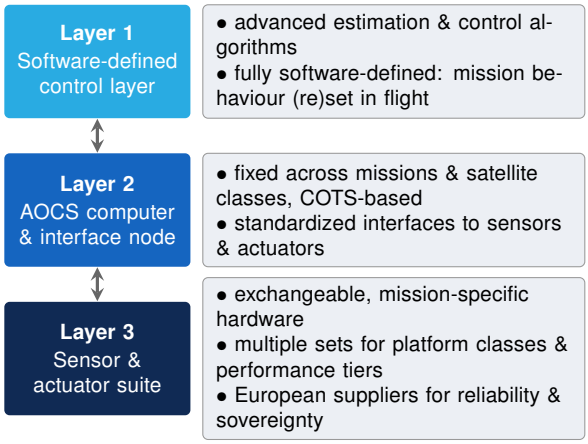

FIG 1. The three layers of the VLEO AOCS (adapted from HAKIV proposal).

2.2. What 'Holistic' Means

In HAKIV, *holistic* combines three properties: coordinated attitude and orbit control that accounts for their coupling and different time scales, hardware-agnostic operation through standardized interfaces, and software-defined mission behaviour that can be adapted without hardware changes. This separates the control intelligence from mission-specific hardware while enabling coordinated control that eliminates the conventional factory separation between attitude and orbit control.

2.3. Three-Layer Architecture

The concept is implemented in three layers, as illustrated in Fig. 1. Layer 1 contains the adaptable, software-defined control and estimation algorithms. Layer 2 is a standardized COTS-based AOCS computer and interface node shared across missions and spacecraft classes. Layer 3 contains exchangeable sensors and actuators selected and scaled according to mission requirements. Thus, Layers 1 and 2 provide the standardized, series-producible core, while Layer 3 accommodates mission-specific hardware.

3. THE ATTITUDE-ORBIT COUPLING PROBLEM

3.1. Coupling Mechanisms

In conventional AOCS design, attitude and orbit control are largely treated as separate problems. In VLEO, this assumption breaks down because both are affected by the same aerodynamic environment, see Fig. 2. Four main coupling mechanisms are relevant. First, the aerodynamic environment couples attitude and orbit disturbances. Atmospheric density and relative velocity determine both drag and aerodynamic torque, so environmental variations

CC BY 4.0

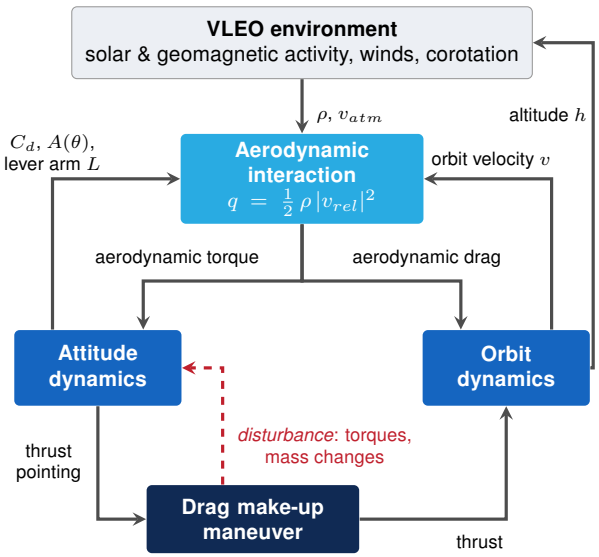

FIG 2. Attitude-orbit coupling in VLEO. Environment (ρ, winds) and orbit state (v_{rel}, h) form one aerodynamic interaction with the attitude set (C_d, $A(\theta)$, d). It projects as drag acceleration into orbit or as drag torque into attitude, drag make-up thrust disturbs the attitude.

affect translational and rotational dynamics simultaneously. Second, attitude affects aerodynamic drag. Spacecraft orientation changes the exposed area and potentially the drag coefficient, directly influencing orbital decay and drag-compensation requirements. Third, the center-of-pressure offset couples drag and attitude. A displacement between the center of pressure and center of mass converts aerodynamic drag into torque, while configuration changes can affect both quantities [6]. Fourth, orbit control affects attitude. Drag-compensation thrust requires accurate pointing and introduces disturbance torques, while propellant consumption changes spacecraft mass properties. In turn, attitude errors can increase drag and accelerate orbital decay [7]. Thus, VLEO attitude and orbit disturbances are physically coupled rather than independent, motivating coordinated control of both domains.

3.2. Consequences for AOCS Design

This coupling makes conventional architectures with independent attitude control and ground-planned orbit control unsuitable for VLEO. Rapid orbital decay and atmospheric variations require autonomous orbit control with a cadence matched to the changing environment. Sharing information between the attitude and orbit controllers allows known effects, such as drag-compensation maneuvers and their reaction torques, to be anticipated rather than treated as disturbances. However, coordination does not require a single controller: attitude and orbit control operate at different time scales, requiring high-rate, short-horizon attitude control and lower-rate, long-horizon orbit control. VLEO therefore calls for coordinated control across these time scales rather than independent subsystem operation.

4. METHOD

4.1. Research Questions

QUEST1 Which are the strongest and most varying environment disturbances in VLEO?

QUEST2 How large are the maximum disturbance torques and forces across VLEO altitudes and platform classes?

QUEST3 At which frequencies do the disturbances occur and what cadence must attitude desaturation as well as orbit correction fulfill?

4.2. Predictive Control as Design Rationale

The coupling analysis demands explicit handling of state and actuator constraints, systematic treatment of environmental uncertainty, and resource-optimal actuation under tight propellant and power budgets – properties optimization-based predictive control provides by construction. One good example in the literature is the work of Mahfouz et al. in [8], who implemented an attitude-orbit coupled Model Predictive Controller (MPC) for autonomous orbit keeping. HAKIV therefore adopts MPC as the algorithmic core of its software control layer, with a short-horizon attitude layer and a long-horizon orbit layer coordinated through a shared disturbance model, reflecting the two-time-scale structure of Sec. 3.2. The specific formulation – prediction model, optimization class, robustness mechanism – remains an open design choice of the ongoing development.
Any such formulation needs disturbance *bandwidths* to set its sampling times and horizon lengths, and disturbance *magnitudes* to set its constraint sets and actuator authority, known across the full altitude band and platform range. MPC is the project's future control method. The simulation presented next only characterizes the disturbance environment and sizes the actuators as preparation for that method, without implementing or evaluating a specific MPC formulation.

4.3. VLEO Environment Simulation

A VLEO disturbance-environment simulation, implemented in MATLAB R2026a, characterizes spacecraft-independent and spacecraft-dependent disturbances across the 200–450 km altitude band for three satellite classes – a 6U CubeSat, a 35 kg baseline SmallSat, and a 100 kg SmallSat. Disturbance torques and translatory accelerations are propagated over a representative number of orbits to define disturbance rejection requirements under worst-case conditions. For the selection of models Traub's work in [2] was crucial. The disturbances to analyze and later plots are based on diagrams used by Fortescue et al. [9], Wertz et al. [10], and Zagorski [11].

CC BY 4.0

Models: NRLMSISE-00 (density), HWM14 (winds), rigid corotation, IGRF (magnetic field), low-precision Sun/Moon ephemerides, single-cone eclipse, WGS84, two-body gravity with J_2-J_5, third-body Sun/Moon gravity, cannonball SRP.
Simplifications: point-mass spacecraft (no geometry, no gas-surface interaction); no attitude propagation, nadir-fixed LVLH attitude and cross-section; constant $C_d = 2.2$, $C_r = 1.3$; binary-cone eclipse; climatological wind; 2° fixed gravity-gradient offset (worst-case nadir pointing error); lever arm fixed in nadir, dipole fixed along-track (both LVLH-corotating); harmonics limited to J_5, no tides or albedo; constant solar activity per run; single epoch; osculating elements.
Disturbances analyzed: translatory accelerations a_{Earth}, a_{J2}-a_{J5}, a_{sun}, a_{moon}, a_{drag}, a_{srp}, a_{total}; torques τ_{aero}, τ_{gg}, τ_{srp}, τ_{mag}, τ_{total}.
Boundary conditions: sun-synchronous orbit, inclination matched per altitude via J_2-nodal precession (standard for EO/COMS in VLEO); eccentricity 0.001, argument of perigee 0°, true anomaly 0° at epoch; RAAN via 11:00 local solar time; epoch spring equinox 2024 (00:00 UTC); nadir-pointing throughout. Self-written propagator, `ode78`, $10^{-8}/10^{-10}$ relative/absolute tolerance.
Classes & sweeps: classes defined by m, A_{ref}, I_{max}, i_{nom}; sweep parameters are solar activity (F10.7, Ap), dimensionless lever arm $\tilde{L}$, inertia $\tilde{I}$, and dipole $\tilde{m}_{dipole}$; see Tab. 1 with Sat1 = 6U CubeSat, Sat2 = 35 kg SmallSat, Sat3 = 100 kg SmallSat.

Satellite parameters	Sat1	Sat2	Sat3
m [kg]	5	35	100
A_{ref} [m^2]	0.05	0.15	0.3
I_{max} [kg m^2]	0.05	0.5	2
i_{nom} [A]	5	10	20
Sweep parameters	low / medium / high		
$\tilde{L} = L/\sqrt{I_{max}/m}$	0.2 / 0.4 / 0.6		
$\tilde{I} = I_{min}/I_{max}$	0.2 / 0.4 / 0.6		
$\tilde{m} = m_{dipole}/(i_{nom} I_{max}/m)$	0.2 / 0.4 / 0.6		
F10.7 [sfu]	65 / 155 / 250		
Ap [-]	4 / 15 / 50		

TAB 1. Satellite and sweep parameters.

5. RESULTS

5.1. Disturbance Environment

Fig. 3 and Fig. 6 characterize the VLEO disturbance environment in two stages: first quantities independent of any spacecraft parameters, then quantities as they are experienced by each of the three satellite classes. Both figures report root mean squared (RMS) values, sampled every 20 km, since RMS is the time-domain equivalent of the signal's total power ($\sigma^2 \approx \int PSD(f)\, df$) and reflects the sustained, average-power level a controller must reject continuously. This is based on Parseval's theorem, see [12]. A plain mean would understate an oscillatory disturbance whose average is near zero, even where its actual amplitude is not.
Spacecraft-independent disturbances: Fig. 3 is computed under conservative dynamics (drag and SRP omitted from the orbit propagator, hence no decay propagation) over 40 orbits per altitude. The dynamic pressure $q = 0.5\rho v^2$ spans roughly three orders of magnitude across the altitude band and is the only quantity here swept over solar activity, since q depends on atmospheric density, which solar extreme ultraviolet light (EUV) heating drives directly, the other channels do not depend on F10.7 (solar radio flux index) or Ap (geomagnetic planetary index) [2]. The zonal harmonics a_{J2}-a_{J5}, third-body a_{sun} and a_{moon} are essentially flat with altitude over this narrow band, since all four depend on distance from Earth's (or the Sun's/Moon's) center, which changes by only a few percent across 200-450 km. a_{J2} dominates the harmonic series by roughly three orders of magnitude, as expected from its quadrupole nature. The geomagnetic field magnitude $|B|$ decreases with altitude, following the expected dipole-like $1/r^3$ falloff [13], while the illuminated fraction increases slightly with altitude, since a higher orbit spends marginally less time in Earth's shadow at fixed inclination and epoch.
Scale-invariant measure of the spacecraft lever arm: The spacecraft-dependent analysis that follows sweeps the CoP-CoM lever arm L across satellite classes, which raises a methodological question first: in which units should L be specified so that its attitude effect is comparable across platforms? In raw units it is difficult to compare – L [m] and the resulting torque τ_{aero} [Nm] both scale strongly with platform size, mixing *how large is the disturbance* with *how large is the satellite*. A dedicated 40-orbit simulation study evaluated two candidate dimensionless numbers on a family spanning 1-500 kg at the altitudes 200, 300, and 400 km.
The first candidate normalizes the offset by the radius of gyration in a purely geometric way, independent of the environment, see Fig. 4:

$$\tilde{L} = L\sqrt{m/I_{max}}. \tag{1}$$

The second follows from linearizing the attitude dynamics: a small pointing perturbation oscillates at the aerodynamic (weathercock [14]) frequency $\omega_a = \sqrt{q\, C_d A_{ref}\, L/I_{max}}$, and comparing it to the orbital mean motion n yields the aerodynamic stiffness ratio, see Fig. 5:

$$\Lambda_{aero} = \left(\frac{\omega_a}{n}\right)^2 = \frac{q\, C_d A_{ref}\, L}{n^2 I_{max}}. \tag{2}$$

This measures the peak aerodynamic torque against the characteristic inertial-orbital torque $n^2 I_{max}$, the same scale governing gravity-gradient torque. A very similar dimensionless quantity is the SRP-analog stiffness ratio with solar radiation pressure P_{srp} and

CC BY 4.0

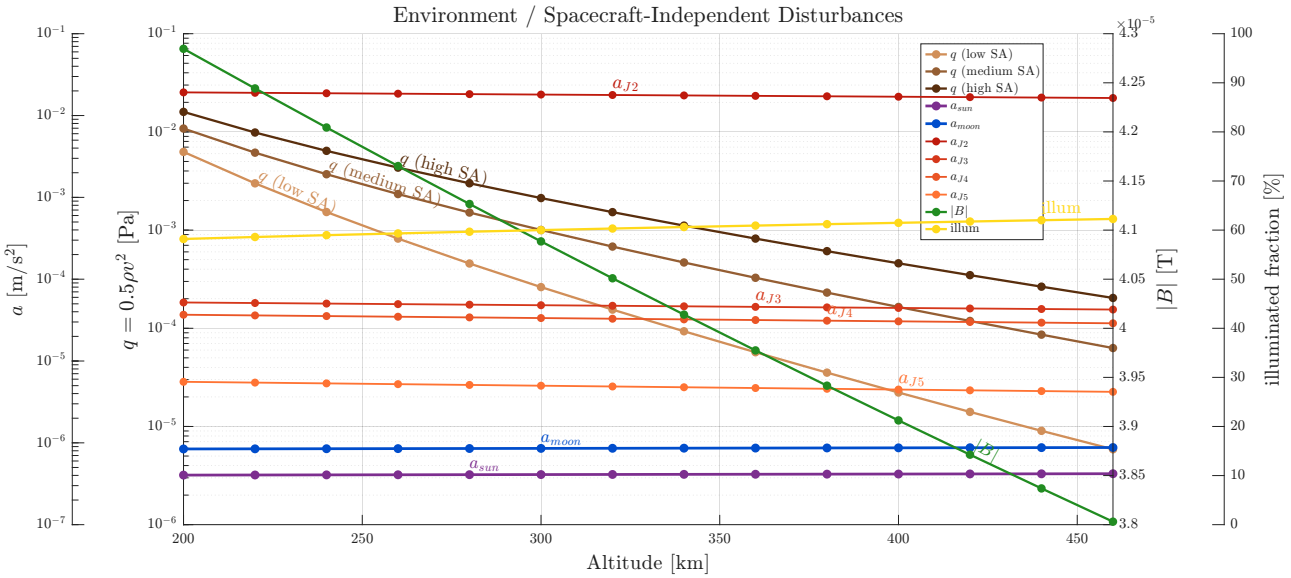

FIG 3. Environment / spacecraft-independent disturbances vs. altitude with solar activity sweep.

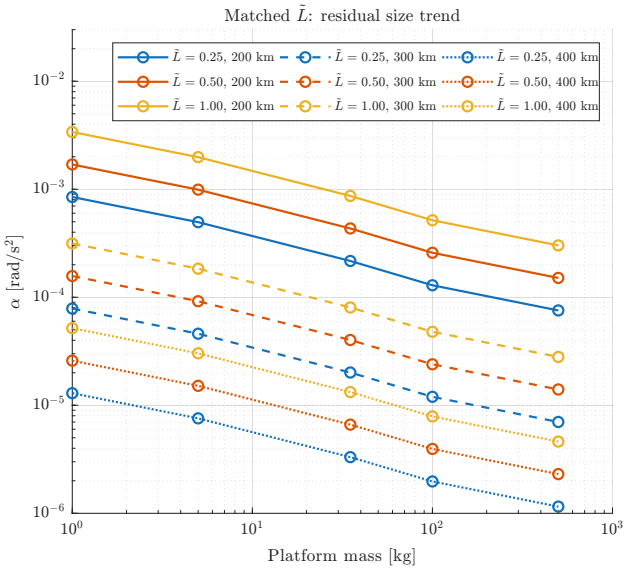

FIG 4. $\tilde{L}$ matched acceleration over altitude; platform/altitude-dependent.

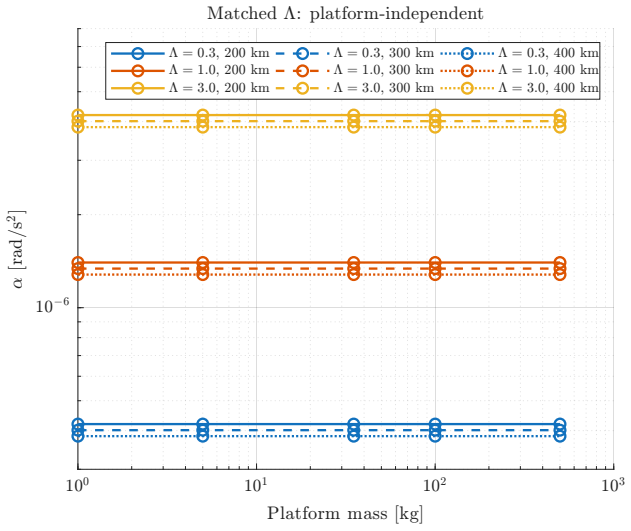

FIG 5. Λ matched acceleration over altitude; platform/altitude-independent.

reflectivity C_r instead of q and C_d:

$$\Lambda_{srp} = \frac{P_{srp}\, C_r A_{ref}\, L}{n^2 I_{max}}. \tag{3}$$

Λ is preferred for a structural reason: the attitude-relevant quantity is $\alpha = \tau_{aero}/I_{max}$, and at fixed $\tilde{L}$ it retains a residual size trend, $\alpha \propto A_{ref}/\sqrt{I_{max}\, m} \propto L^{-2}$, since area and inertia scale differently and the radius of gyration cannot reconcile them – smaller platforms are intrinsically more sensitive to the same relative offset, see higher accelerations for lower masses in Fig. 4. Fixing Λ instead fixes $\alpha = n^2\Lambda$ exactly, and the response collapses onto platform-independent lines as you can see in Fig. 5. Λ additionally collapses the response across altitude within VLEO: its residual altitude-dependence enters only through n^2, which varies by under 10% over 200-400 km, in contrast to q's roughly three-order-of-magnitude variation over the same band – a result specific to VLEO's narrow altitude range, not a general property of Λ. Λ therefore places any VLEO platform on a single scale-invariant axis and is the preferred quantity for *comparing* the aerodynamic disturbance across classes, since $\tau_{aero}/(n^2 I_{max})$ equals Λ_{aero} by construction.

Its value against the threshold $\Lambda = 1$ directly tells whether aerodynamic torque dominates over the inertial torque ($\Lambda > 1$) for a given class, altitude, and design point or not ($\Lambda < 1$). Λ's comparative usefulness does not carry over to actuator sizing. A Λ-matched sweep, by definition, holds the disturbance at a chosen target value and allows solving for the offset L that produces it. The resulting curve is flat because the target was flat, not because the underlying disturbance is. Sizing an actuator instead requires the genuine, as-simulated torque magnitude

CC BY 4.0

at each class and altitude, unmatched to any target. The spacecraft-dependent analysis that follows therefore returns to altitude as the common axis and applies only $\tilde{L}$-matching with radius of gyration Eq. (1) to Sat1, Sat2, and Sat3.

Spacecraft-dependent disturbances: In Fig. 6 the panels sweep satellite class rather than solar activity, at fixed medium solar activity conditions, since the purpose here is to expose how the disturbances scale with spacecraft parameters rather than with the environment. Both panels are computed under the same conservative, 40-orbit dynamics as Fig. 3.

In the top panel a_{drag} increases by roughly two orders of magnitude with decreasing altitude, tracking q from Fig. 3, and separates most strongly for the CubeSat, which has the lowest ballistic coefficient and is therefore most sensitive to density. a_{srp} is nearly flat with altitude at $\sim 10^{-8}$ m/s^2 and very similar across classes, since solar radiation pressure depends only on the area-to-mass ratio and illumination geometry, neither of which varies strongly. The decay rate $|\dot{a}|$, also increasing by roughly two orders of magnitude toward lower altitude, requires a genuinely different simulation than a_{drag} or a_{srp}: it by definition requires the orbit to actually decay, so it is computed under real dynamics over 80 orbits at high solar activity conditions for different initial altitudes. Since the used density model cuts off at 120 km altitude, the satellite classes do not complete all 80 orbits from a certain initial altitude downward. The decay-rate estimate is then a linear fit over fewer orbits than at higher altitudes, visible as the kinks/bends in the plot – for Sat1 at 280 km, for Sat2 at 240 km, and for Sat3 at 220 km.

The bottom panel shows aerodynamic torque τ_{aero}, normalized by $n^2 I_{max}$, plotted against the dimensionless lever arm $\tilde{L}$ from Eq. (1), swept at three levels per class. This dimensionless form is chosen as described in the sclae-invariant analysis above to separate how torque scales with design choice and altitude on a common ground across classes. Without we would mostly see the effect of mass and inertia difference between classes. $\Lambda_{aero} = \tau_{aero}/(n^2 I_{max})$ scales with $\tilde{L}$ and spans roughly two orders of magnitude from 200 to 460 km. It is highest for Sat1 and lowest for Sat3, since a small class's I_{max} in the denominator outweighs its smaller absolute torque in the numerator. The horizontal $\Lambda = 1$ line shows that only the dimensionless torques of Sat3 with $\tilde{L} = 0.2$ or $\tilde{L} = 0.4$ and of Sat2 with $\tilde{L} = 0.2$ go below the threshold around 420 and 450 km, where inertial torque dominates over aerodynamic. Only where the aerodynamic torque dominates, the disturbance torque is relevant for actuator sizing.

The remaining three torque channels – gravity-gradient τ_{gg}, magnetic τ_{mag}, and solar radiation pressure τ_{srp} – are not plotted, since each is essentially constant across the altitude band. Their approximate dimensionless magnitudes Λ per class are reported in Tab. 2 instead.

Torque/Class	Sat1	Sat2	Sat3
Λ_{srp}	$\sim 10^{-1}$	$\sim 10^{-2}$	$\sim 10^{-2}$
Λ_{gg}	$\sim 10^{-2}$	$\sim 10^{-2}$	$\sim 10^{-2}$
Λ_{mag}	$\sim 10^{1}$	$\sim 10^{0}$	$\sim 10^{0}$

TAB 2. Approximate dimensionless magnitudes of non-plotted torques $\Lambda = \tau/(n^2 I_{max})$.

5.2. Disturbance Rejection Requirements

This section derives the disturbance rejection requirements based on Figs. 7 to 9 and Tab. 3.

5.2.1. Peak Torque and Thrust

Fig. 7 reports *peak* torque and along-track thrust per altitude, since actuator authority must cover the instantaneous maximum. It is computed under high solar activity and conservative dynamics (no decay propagation) over 40 orbits, sampled every 20 km. Both curves grow steeply toward low altitude – visually close to exponential even on the already-logarithmic axis – since peak drag-driven torque and thrust inherit the density profile's own steep altitude dependence. Peak torque and thrust have roughly a two magnitudes range for each satellite class over the VLEO altitude band. These are not normalized values, so the CubeSat shows the lowest absolute peaks and the 100 kg SmallSat the highest, tracking mass and reference area directly. The attitude and orbit control requirement REQ1 follows from it with altitude h and satellite class c.

REQ1 *Peak attitude/orbit control authority.* The attitude and orbit control system must supply at least the simulated peak vector sum torque and along-track thrust under worst-case (high solar activity) conditions:

(4)
$$\tau_{req}(h,c) \geq \tau_{peak}(h,c), \quad F_{req}(h,c) \geq F_{peak}(h,c).$$

5.2.2. Control Bandwidth

Bandwidth is derived from each disturbance signal's power spectral density (PSD) as the frequency below which 95% of cumulative spectral power is contained (bw_{95}). The resulting control bandwidth is taken as $10 \times bw_{95}$. Torque bandwidth is computed from the magnitude sum of the four torque channels, chosen over the vector sum to avoid partial torque counteractions and hence potential frequency band cancellations. This would produce a vector sum PSD with artifacts unsuitable as an actuator sizing basis. Non-conservative (drag & SRP) acceleration bandwidth is computed from the vector sum, since they don't counteract or cancel each other.

Tab. 3 summarizes both. Solar activity is the dominant driver in both cases. Satellite class causes only minor variation within a given solar-activity level. Torque bandwidth shows one drop per solar activity level, from 7.3×10^{-3}Hz in higer to 3.9×10^{-3} Hz in

CC BY 4.0

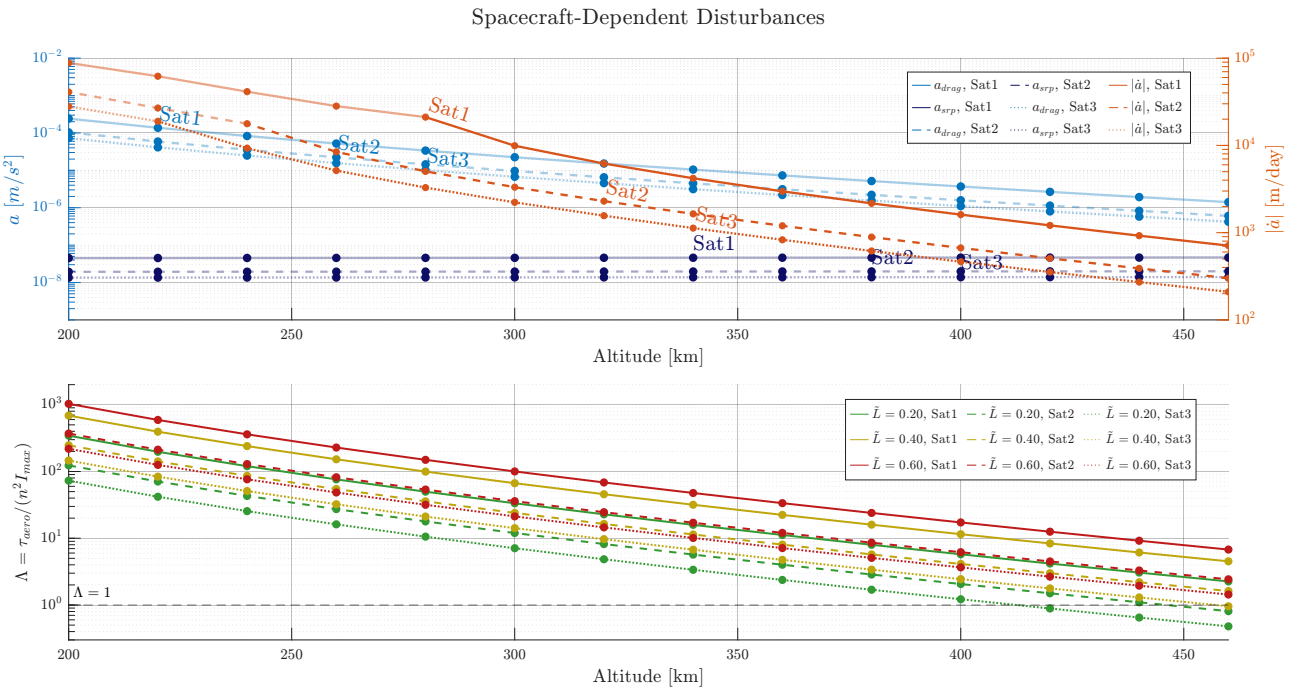

FIG 6. Spacecraft-dependent disturbances vs. altitude with three different satellite classes.

lower altitudes. The drop is associated with a switch in dominant torque channel from magnetic to aerodynamic, which occurs at different altitudes for different solar activity levels. The reason is that magnetic torque comes from a cross product of two orbital rate dependent quantities that produce a higher harmonic content, leading to the counterintuitve hiher bandwidth in higher orbits. Low solar activity pushes the same regime change to lower altitude. Drag-and-SRP acceleration bandwidth shows the opposite altitude trend. Lower frequency (3.6×10^{-3} Hz) at higher altitude, rising to 3.9×10^{-3} Hz below a single transition near 400-350 km for all classes and solar-activity levels.
The attitude control requirement REQ2 follows from it with solar activity SA.

REQ2 *Attitude control bandwidth.* The attitude loop must achieve a control bandwidth of at least ten times the 95%-power bandwidth $bw_{95,\tau}$ of the magnitude sum disturbance torque PSD:

(5) $$BW_{ctrl,\tau}(h, c, SA) \geq 10 \times bw_{95,\tau}(h, c, SA).$$

Channel	SA	$f_{high-alt}$	$f_{low-alt}$	Transition
τ_{total}	high	7.3	3.9	450-400 km
(magnitude	medium	$\times 10^{-3}$	$\times 10^{-3}$	350-300 km
sum)	low	Hz	Hz	300-260 km
$a_{drag+srp}$	high	3.6	3.9	
(vector	medium	$\times 10^{-3}$	$\times 10^{-3}$	400-350 km
sum)	low	Hz	Hz	

TAB 3. Disturbance bandwidth bw_{95} and transition altitude by channel & solar activity (SA).

5.2.3. Angular Momentum Capacity

Fig. 8 plots momentum capacity $H(T_{sat})$ – the sliding-window maximum accumulated vector sum torque – against saturation window T_{sat}, from 1 s to one orbital period (∼5500 s), under conservative 40-orbits dynamics at medium solar activity. For a reaction wheel of rated momentum capacity H_{sat}, the maximum desaturation interval it supports is defined by the attitude requirement REQ3.

REQ3 *Momentum storage time.* For a reaction wheel selected through REQ1, the maximum saturation interval $T_{sat(uration)}$ must not exceed the wheel's sliding-window accumulated vector sum torque $H_{sat(uration)}$ over that interval:

(6) $$T_{sat}(h, c; H_{sat}) = \max\{T : H(T; h, c) \leq H_{sat}\}.$$

The inverse $f_{desat} = 1/T_{sat}$ is directly comparable to the torque bandwidths of Tab. 3. As with REQ1, REQ3 does not resolve to a single value from the disturbance analysis alone. H_{sat} is a hardware property, and Eq. (6) states the relationship a wheel would be evaluated against. Tab. 4 reports the disturbance at a fixed reference window of half an orbit. This is illustrative, but a concrete, class- and altitude-comparable read of Fig. 8 without hardware assumption/selection.

Class	200 km	300 km	400 km
Sat1	143.04	15.01	3.94
Sat2	511.97	52.74	12.67
Sat3	1212.77	126.29	32.13

TAB 4. Accumulated momentum $H\,[mNms]$ at a half-orbit reference window $T \approx 2750\,s$.

CC BY 4.0

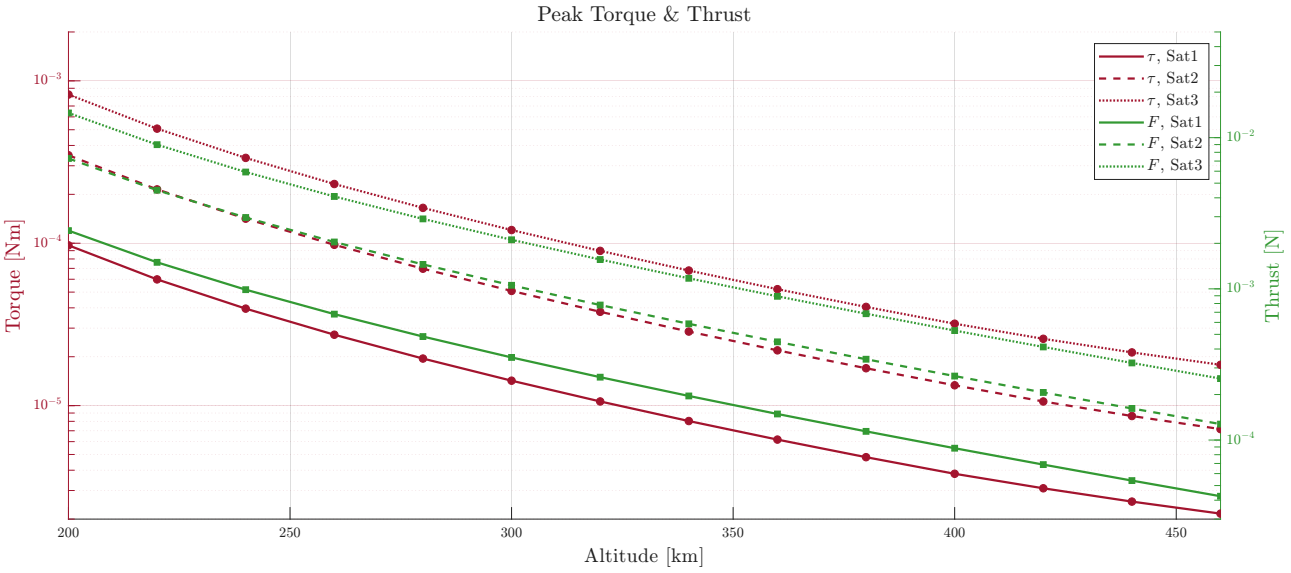

FIG 7. Peak torque and thrust vs. altitude.

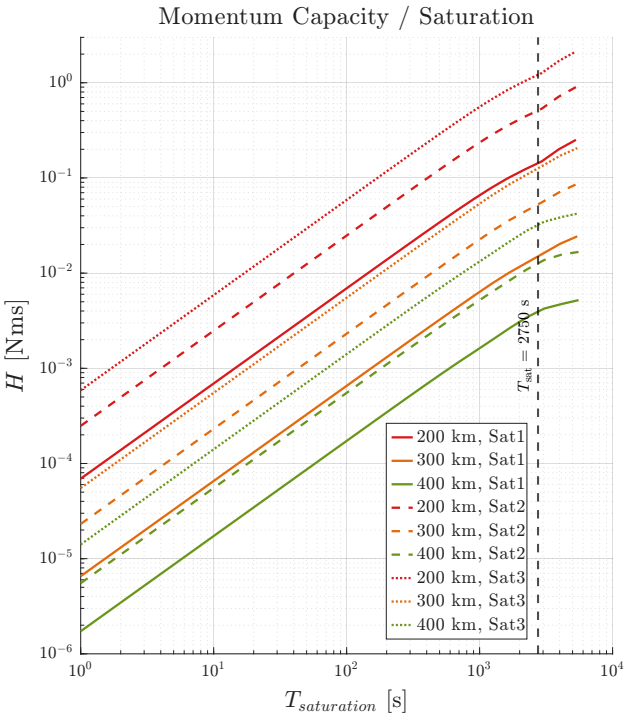

FIG 8. Momentum capacity vs. saturation window at 200, 300, and 400 km.

Class	Altitude	T_{ctrl} [s]	f_{ctrl} [mHz]	Δv_{ctrl} [m/s]
Sat1	200 km	11	90.9	0.366
Sat1	300 km	306	3.27	0.0131
Sat1	400 km	857	1.17	4.638
Sat2	200 km	3	333.3	0.0597
Sat2	300 km	117	8.55	1.716
Sat2	400 km	292	3.43	6.84
Sat3	200 km	3	333.3	0.0148
Sat3	300 km	64	15.6	6.3
Sat3	400 km	156	6.41	2.56

TAB 5. Control interval, control frequency, and required Δv per cycle, by class and altitude.

5.2.4. $\Delta v/\Delta s$ Capacity and Control Interval

Fig. 9 plots accumulated Δv and Δs – sliding-window single and double integrals of the non-conservative along-track disturbance acceleration's vector sum – against control window T_{ctrl}, from 3 s to one orbital period (∼5500 s), under real (decaying) 80-orbit dynamics at medium solar activity for the altitudes 200, 300, and 400 km. An orbit-determination (OD) precision value per class is overlaid on Δs, reflecting a structural fact and not a hardware limitation: orbit decay is slow and orbit determination imprecise, so some time must pass and some drift must accumulate before a correction is even detectable, let alone worth executing. This is the orbit control's minimum control interval, or maximum control cadence. Where the disturbance curve crosses the orbit-determination line marks the minimum control interval T_{ctrl}. The corresponding Δv_{ctrl} is read off the Δv curve at that same T_{ctrl}. Tab. 5 reports the resulting T_{ctrl}, the maximum control frequency $f_{ctrl} = 1/T_{ctrl}$, and the minimum Δv_{ctrl} for every class and altitude. The orbit-control requirement REQ4 follows directly from Fig. 9 and Tab. 5.

REQ4 *Maximum orbit correction cadence and impulse capacity.* The achievable control interval is bounded by orbit-determination precision $\delta_{OD}(c)$:

$$T_{ctrl}(h,c) = \min\{T : \Delta s(T;h,c) \geq \delta_{OD}(c)\} \tag{7}$$

with the resulting minimum impulse requirement Δv_{req} per correction cycle at that same T_{ctrl}:

$$\Delta v_{req}(h,c) = \Delta v\big(T_{ctrl}(h,c);h,c\big). \tag{8}$$

CC BY 4.0

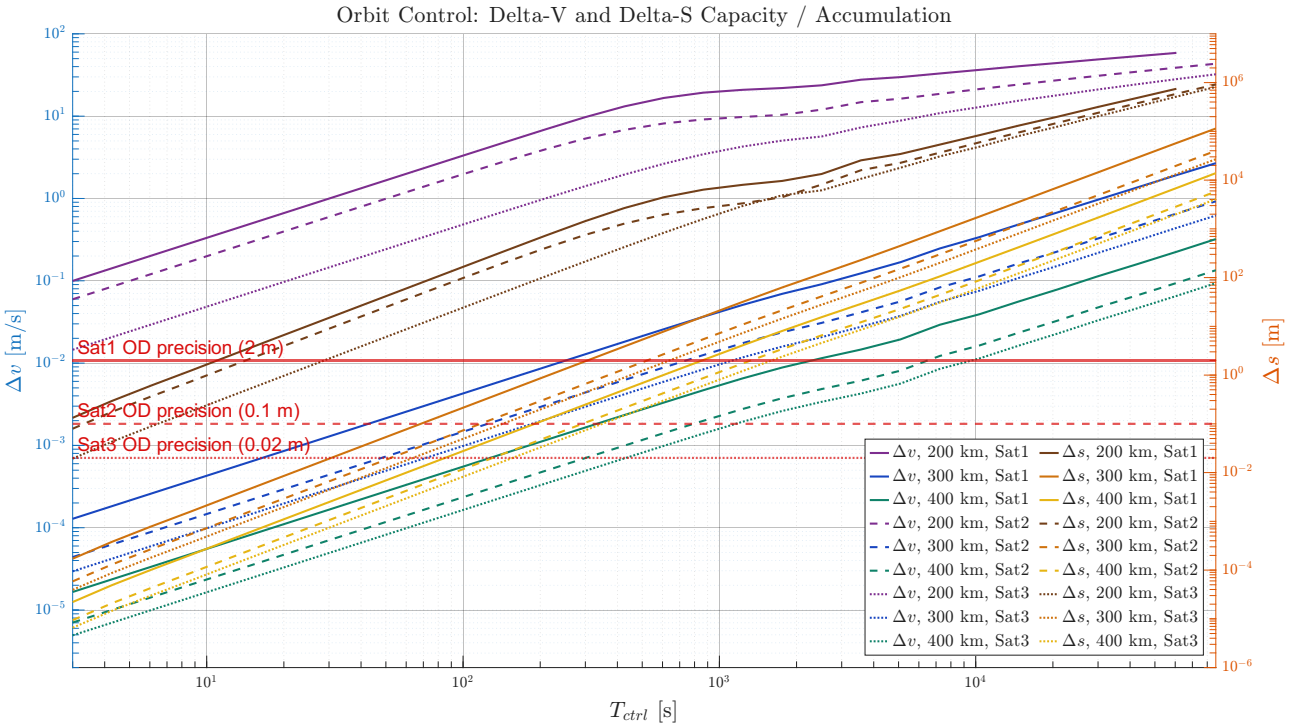

FIG 9. $\Delta v/\Delta s$ accumulation vs. control interval, with orbit-determination precision overlays.

6. CONCLUSION

6.1. Summary

This paper set out to answer three questions about the VLEO disturbance environment and the demands it places on a small satellite VLEO AOCS.

To answer QUEST1, the aerodynamic effects dominate. Dynamic pressure spans roughly three orders of magnitude across 200–450 km and is the environment's single most sensitive quantity du to solar activity, driving comparable variation in drag acceleration, decay rate, and aerodynamic torque (Figs. 3 and 6). The remaining environmental channels – gravity harmonics, third-body gravity, the geomagnetic field, illumination – vary by only a few percent across the same altitude band and are effectively constant by comparison.

To answer QUEST2, the peak torque ranges from 2×10^{-6} to 8×10^{-4} Nm, and the peak thrust from 4×10^{-5} to 1×10^{-2} N across the three platform classes and the 200–450 km band (Fig. 7). They scale with mass and reference area as expected. The 100 kg SmallSat sees roughly an order of magnitude higher peaks than the CubeSat at the same altitude.

To answer QUEST3, the disturbance torque bandwidth ranges from 3.9×10^{-3} to 7.3×10^{-3} Hz depending on the switch from magnetic to aerodynamic dominance and on the solar activity, shifting the switch to lower altitude with lower solar activity level. Drag-and-SRP acceleration bandwidth ranges $3.6\text{-}3.9 \times 10^{-3}$ Hz, with the opposite altitude trend (Tab. 3). The reaction wheel desaturation cadence depends on selected actuators' maximum angular momentum. While the orbit correction cadence has an upper boundary defined by orbit determination accuracy that sets the minimum detectable drift (Tabs. 4 and 5).

These findings are consolidated into four rejection requirements, derived from the disturbance analysis: REQ1, REQ2, and REQ4 resolve directly to a value from the disturbance analysis and the chosen measurement method, independent of any specific actuator. REQ3 is the exception: momentum storage capacity is inherently a hardware property with no environment- or measurement-based analog, so it is stated here as the general relationship a wheel selection would be evaluated against, not a resolved number.

6.2. Outlook

This paper deliberately stops at the rejection requirements, before selecting specific hardware – a scope decision made to keep the analysis a disturbance characterization rather than a design exercise. But to complete the disturbance characterization, a thourough uncertainty quantification or prediction, especially of the solar activity's influence, must be conducted. The next step after the uncertainty quantification is the actuator sizing process. REQ1 and REQ3's own structure indicate what it requires: peak torque/thrust and momentum storage margins sized purely against disturbance rejection are not sufficient for actuator selection on their own, since real actuators must also execute deliberate maneuvers – attitude slews at a required agility/rate, and orbit corrections recovering from a maximum allowable deviation within a bounded time. This requires impulsive or continuous Δv beyond the

CC BY 4.0

disturbance-driven Δv_{ctrl} of REQ4. A margin derived from these technical maneuver requirements, rather than an assumed multiplicative factor on disturbance alone, is the natural refinement of REQ1 and REQ3 for the next stage of this work.
Once thrusters are selected against that refined requirement, REQ4's cadence result feeds directly into a mission duration estimate from total impulse: $T_{mission} = T_{ctrl} \cdot I_{total}/(m \cdot \Delta v_{ctrl})$. REQ4's OD-based cadence assumes a scheduled correction architecture, a continuous-thrust architecture, sustained low-level correction rather than discrete scheduled burns, will be one of the next analyses regarding propulsion and control. Such an architecture removes the impulse-resolution question and shifts the constraint to the disturbance-sensing side, since a continuously-acting controller needs a correspondingly fast disturbance estimate. Orbit determination reveals disturbance indirectly, direct accelerometer-based measurement of drag and SRP acceleration is one of the next investigations to conduct.

ACKNOWLEDGMENTS

This research is conducted by Technical University of Berlin (TUB) and EnduroSat GmbH (ES), funded by the German Space Agency at DLR under support code 50RK2605B.

Contact address:

b.jaeger@tu-berlin.de

References

[1] N. H. Crisp, P. C. E. Roberts, S. Livadiotti, V. T. A. Oiko, S. Edmondson, S. J. Haigh, et al. The benefits of very low earth orbit for earth observation missions. *Progress in Aerospace Sciences*, 117:100619, 2020. DOI: 10.1016/j.paerosci.2020.100619.

[2] C. Traub. *Differential Aerodynamic Forces as a Means to Control Satellite Formation Flight*. PhD thesis, University of Stuttgart, Institute of Space Systems, 2022. TODO verify: exact title and year.

[3] G. Sechi, G. André, D. Andreis, and M. Saponara. In-flight results from the drag-free and attitude control of GOCE satellite. In *18th IFAC World Congress*, pages 733–740, Milano, Italy, 2011. DOI: 10.3182/20110828-6-IT-1002.02966.

[4] D. A. Vallado. *Fundamentals of Astrodynamics and Applications*. Microcosm Press, Hawthorne, CA, 4th edition, 2013. ISBN: 978-1881883180.

[5] D. González, V. Cañas, J. Becedas, R. M. Domínguez, T. Ramio, P. C. E. Roberts, N. H. Crisp, et al. Modelling and simulation of very low earth orbits. In *8th European Conference for Aeronautics and Space Sciences (EUCASS)*, Madrid, Spain, 2019. Paper 176.

[6] J. Virgili-Llop, H. C. Polat, and M. Romano. Attitude stabilization of spacecraft in very low earth orbit by center-of-mass shifting. *Frontiers in Robotics and AI*, 6(7), 2019. DOI: 10.3389/frobt.2019.00007.

[7] F. Zhang and G. Duan. Integrated modeling and control of spacecraft coupled orbit and attitude dynamics. *IEEE/CAA Journal of Automatica Sinica*, 10(12):2187–2208, 2023.

[8] Ahmed Mahfouz, Gabriella Gaias, D. M. K. K. Venkateswara Rao, and Holger Voos. Autonomous optimal absolute orbit keeping through formation flying techniques. *Aerospace*, 10(11), 2023. DOI: 10.3390/aerospace10110959.

[9] P. Fortescue, G. Swinerd, and J. Stark. *Spacecraft Systems Engineering*. John Wiley & Sons, Chichester, UK, 4th edition, 2011. ISBN: 978-0470750124.

[10] James R. Wertz, David F. Everett, and Jeffery J. Puschell. *Space Mission eEngineering : The New SMAD*. 2011.

[11] P. Zagórski. Modeling disturbances influencing an earth-orbiting satellite. *Pomiary Automatyka Robotyka*, 16(5):98–103, 2012.

[12] M.-A. Parseval des Chenes. Mémoire sur les séries et sur l'intégration complète d'une équation aux différences partielles linéaire du second ordre, à coefficients constants. *Mémoires présentés à l'Institut des Sciences, Lettres et Arts, par divers savants, et lus dans ses assemblées. Sciences, mathématiques et physiques. (Savants étrangers.)*, 1(1806):638–648, 1799.

[13] X. Borg. The inverse cube law for dipoles. *The General Science Journal*, 2009.

[14] Ariane Gayout, Ármann Gylfason, Nicolas Plihon, and Mickaël Bourgoin. Fluidelastic modeling of a weathercock stabilization in a uniform flow. *Journal of Fluids and Structures*, 120:103895, 2023. DOI: 10.1016/j.jfluidstructs.2023.103895.

CC BY 4.0